PAPER

Check for updates

Efficient asymmetrical silicon–metal dimer electrocatalysts for the nitrogen reduction reaction†

Chuangwei Liu, [ID] [a] Haoren Zheng,[a] Tianyi Wang,[ab] Xiaoli Zhang,[c] Zhongyuan Guo [ID] *[b] and Hao Li [ID] *[b]

The electrocatalytic nitrogen reduction reaction (ENRR) has been regarded as an eco-friendly and feasible substitute for the Haber–Bosch method. Identifying the effective catalysts for the ENRR is an extremely important prerequisite but challenging. Herein, asymmetrical silicon–metal dimer catalysts doped into g-C_3N_4 nanosheets with nitrogen vacancies (SiM@C_3N_4) were designed to address nitrogen activation and reduction. The concept catalysts of SiM@C_3N_4 can combine the advantages of silicon-based and metal-based catalysts during the ENRR. Among the catalysts investigated, SiMo@C_3N_4 and SiRu@C_3N_4 exhibited the highest activities towards the ENRR with ultra-low onset potentials of −0.20 and −0.39 V; meanwhile, they suppressed the competing hydrogen evolution reaction (HER) due to the relative difficulty in releasing hydrogen. Additionally, SiRu@C_3N_4 is demonstrated to possess strong hydrophobicity, which is greatly beneficial to the production of ammonia. This research provides insights into asymmetrical silicon–metal dimer catalysts and reveals a new method for developing dual-atom electrocatalysts. This asymmetrical dimer strategy can be applied in other electrocatalytic reactions for energy conversion.

1. Introduction

The electrocatalytic nitrogen reduction reaction (ENRR) has been considered to be the most promising route for artificial N_2 fixation under ambient conditions, as it can convert N_2 into NH_3 using renewable energy sources (wind and solar energies) on the surface of electrocatalysts.[1–5] Although tremendous efforts have been made, the performance of electrocatalysts as the core part of electrocatalytic systems is still far from that required for realizing a pragmatic application.[6] Now, our societies rely heavily on the century-old Haber–Bosch (HB) method for industrial NH_3 production, which consumes considerable energy and releases a tremendous amount of CO_2 annually.[7] To cope with the global energy crisis and climate change, high-performance ENRR catalysts are urgently needed to substitute for the HB route.

In recent years, metal-free ENRR catalysts have been attracting attention due to their application potential.[3,5,8–14] Unlike metal-based electrocatalysts, metal-free electrocatalysts can circumvent the intrinsic shortcoming of the strong *H affinity on metal-based ones, which is conducive to increasing Faradaic efficiency (FE). Moreover, metal-free electrocatalysts possess the advantages of low cost and high modification versatility, which make them suitable for pragmatic applications. For example, Sun *et al.*[15–18] experimentally modified carbon-based materials *via* O, F, and S heteroatoms for N_2 electroreduction to NH_3 and achieved comparable performance with that of metal-based electrocatalysts. In addition, metal-free Si-based catalysts have begun to arouse research interests in relation to the ENRR. For instance, Li *et al.*[19] experimentally investigated atomically dispersed Si atoms on carbon nanolayers for N_2 fixation and found that isoelectric Si heteroatoms can function as metal-free single-atom-based catalysts to greatly improve the FE of the pristine carbon support, with comparable results to atomically dispersed metal-based catalysts. Our previous studies also investigated the potential of Si-based electrocatalysts for the ENRR from a theoretical viewpoint, of note,[13,20,21] finding the relatively lower affinity of N_2 on Si sites compared with that on transition metal sites, which could adversely affect the subsequent activation and hydrogenation of *N_2. However, low-coordination Si atoms can act as a Lewis acid to interact with

[a] *Key Lab for Anisotropy and Texture of Materials, School of Materials Science and Engineering, Northeastern University, Shenyang 110819, China*

[b] *Advanced Institute for Materials Research (WPI-AIMR), Tohoku University, Sendai 980-8577, Japan. E-mail: zhongyuanguo2022@163.com, li.hao.b8@tohoku.ac.jp*

[c] *School of Material Science and Engineering, Zhengzhou University, Zhengzhou 450001, China*

13126 | *Phys. Chem. Chem. Phys.*, 2023, **25**, 13126–13135

This journal is © the Owner Societies 2023

N_2 as a Lewis base with under-occupied p-orbitals *via* an electron acceptance-donation process.[22] Compared with the carbon atom sites on the carbon-based catalysts mentioned above, the lower electronegativity of Si can contribute to more electron back-donation into the $1\pi^*$ anti-bonding orbitals of $^*N_2$.

The atomically dispersed dual-atom catalysts (DACs) have garnered extensive research interest in heterogeneous catalysis due to their unique electronic structures, maximum atom-utilization efficiencies, and flexible reaction sites.[23–25] Especially, the heteronuclear DACs with asymmetric active sites, as a new rising star, have opened a novel pathway in atomic catalysis, which will advance the material design to address critical challenges in energy conversion. For example, Wang *et al.* designed heteronuclear DACs to break through the restriction of scaling relations on CO_2 catalytic activity by combining two kinds of metal atoms embedded in the 2D C_2N support.[26] Moreover, Du *et al.* proposed metal Cu and non-metal B atoms supported on $g\text{-}C_3N_4$ (Cu-B@$g\text{-}C_3N_4$) for CO dimerization, which effectively reduced the CO dimerization free energy barrier due to the asymmetric synergy of the Cu–B center and suppresses the parasitic hydrogen evolution reaction (HER) caused by the synergistic d_{Cu}–p_B coupling.[27] Therefore, based on the aforementioned discussions, in this work, we hypothesized that the dual-atom silicon (Si)–metal (M) dimers on supports could be a viable way to increase the affinity of N_2 on catalysts and achieve an excellent catalytic performance in the ENRR on an asymmetric active center. The chosen supporter was $g\text{-}C_3N_4$ due to its facile synthesis methods, large surface, and porous structure.[28] And $g\text{-}C_3N_4$ has been widely employed in photocatalysis and electrocatalysis.[29–35] More importantly, as for Si–M dimers, the comparably easily formed N vacancy sites (N_V) during the synthesis of $g\text{-}C_3N_4$ are suitable anchoring sites, and have been reported to facilitate electrocatalysis on doped $g\text{-}C_3N_4$.[36–38] Based on previous reports on efficient metal-based catalysts for the ENRR,[39–46] here we selected Fe, Co, Ni, Nb, Mo, Ru, Rh, W, and Re metal atoms for the design of the Si–M dimer on $g\text{-}C_3N_4$. The finally designed dimer catalysts were denoted as SiM@C_3N_4, and the corresponding single-atom Si/M-doped catalysts were denoted as Si@C_3N_4 or M@C_3N_4 (more information regarding the catalyst models is provided in the ESI†). After comprehensive calculations, it was found that the asymmetric dimer catalysts (SiM@C_3N_4) can not only improve the capture of N_2 in the horizontal mode but also boost the subsequent hydrogenation process. Among the concept catalyst models, SiMo@C_3N_4 and SiRu@C_3N_4 are demonstrated to have ultra-low onset potentials of -0.20 and -0.39 V, respectively, towards the ENRR. Meanwhile, the HER would be suppressed on these two dimer catalysts due to larger free-energy barriers for H_2 release from active sites ($^*H + H^+ + e^- \rightarrow H_2$). This work for the first time explores asymmetrical dimer catalysts composed of metals and non-metals for the ENRR, which not only combine the advantages of two types of external atoms but also offer a novel avenue for designing high-performance artificial N_2 fixation catalysts.

2. Calculation details

Spin-polarized density functional theory (DFT) calculations were performed using the DMol^3 code to study the structure properties of Si–M dimers on $g\text{-}C_3N_4$ and their corresponding ENRR activity. The revised Perdew–Burk–Ernzerhof (RPBE) generalized gradient approximation (GGA) was used to describe the electron exchange–correlation. The DFT semi-core pseudo-pots (dspp) pseudopotentials and double numerical basis sets with polarization functions (DNP) were adopted in all calculations. The Tkatchenko–Scheffler (TS) scheme was employed to illustrate the van der Waals (VDW) interactions between catalysts and adsorbates.[47] The real-space global cutoff radius was set to be 5.2 Å. A ($3 \times 3 \times 1$) *k*-point set within the Monkhorst–Pack scheme was used to sample the Brillouin zone. Moreover, the solvation effect was also considered using the COSMO scheme with an H_2O dielectric constant of 78.54 for the ENRR. All structural optimizations were performed until the energy tolerance and residual force were smaller than 10^{-5} Ha and 0.002 Ha Å^{-1}, respectively, and SCF tolerance was set as 10^{-6} Ha. On the basis of the computational hydrogen electrode (CHE) model developed by Nørskov *et al.*,[48,49] the free energy of each elementary reaction at 298.15 K and pH = 0 without the extra potential was calculated as follows:

$$\Delta G = \Delta E_{DFT} + \Delta E_{ZPE} - T\Delta S$$

where ΔE_{DFT}, ΔE_{ZPE}, and ΔS are the differences in the total electronic energy (E_{DFT}), zero-point vibration energy (E_{ZPE}), and entropy (S), respectively. The E_{ZPE} value can be obtained from the harmonic frequency analyses, where only the reaction intermediates (N_xH_y) were taken into account for the calculation of partial Hessian. The entropy of the adsorbed intermediates was negligible in comparison with that of the free gas molecules (H_2, N_2 and NH_3). From the free energy evolution of the ENRR, one can evaluate the activity of catalysts. The limiting potential (U_L) of the ENRR was calculated as $U_L = -\Delta G_{max}/e$, which represents the potential required to eliminate the potential-determining step (PDS). Then overpotential (η) can be calculated from $\eta = U_e - U_L$, where U_e is the equilibrium potential of the NRR ($U_e = -0.16$ V *vs.* standard hydrogen electrode). Of note, here ΔG_{max} comes from the hydrogenation or the proton-coupled electron transfer step, and not the release step of NH_3, because the formed NH_3 could be easily converted into NH_4^+ in acidic electrolytes and desorbed from active sites smoothly according to relevant reports.[50] The charge density difference of the system (AB) was calculated from $\Delta\rho = \rho_{AB} - \rho_A - \rho_B$, where ρ_{AB}, ρ_A, and ρ_B are three different charge density quantities and the atomic positions were fixed as those in the AB system when calculating the latter two quantities. The complete LST/QST protocol and CI-NEB method were used to locate the transition state (TS) for the reaction barrier analysis.[51] When calculating the density of states (DOS) and the crystal orbital Hamiltonian population (COHP), the ($6 \times 6 \times 1$) *k*-point set was used to sample the Brillouin zone.

This journal is © the Owner Societies 2023

Phys. Chem. Chem. Phys., 2023, **25**, 13126–13135 | **13127**

3. Results and discussion

3.1 N₂ adsorption and reduction on Si@C₃N₄

Before examining the ENRR performance of SiM@C₃N₄, we started with investigating the N₂ adsorption and reduction on single-atom Si-doped g-C₃N₄ (Si@C₃N₄) for comparison purposes with the subsequent studies on SiM@C₃N₄. In g-C₃N₄, there are three types of N sites, as shown in Fig. 1a. According to the relevant report on defective g-C₃N₄,[31,52] N_{v1} is the common and easily formed defective site on the plane of g-C₃N₄, which is an ideal anchoring site for heteroatom doping. Therefore, a single-atom Si heteroatom is embedded into this defect and then the designed Si@C₃N₄ is optimized, as shown in Fig. 1a for the subsequent calculations and comparative analysis. According to the binding energy (E_b) equation: $E_b = E_{cat.} - E_{Si} - E_r$, where $E_{cat.}$, E_{Si}, and E_r represent the total electronic energies of the catalyst designed, atomic Si in the gas phrase, and the remaining part of the catalyst with atoms constrained in the lattice position, we obtained $E_{b,Si} = -6.51$ eV on g-C₃N₄, suggesting the strong binding strength of Si on the defective g-C₃N₄ catalyst. Then compared with the cohesive energy of Si ($E_{co,Si} = -4.55$ eV), one can see the excellent stability of single-atom Si@C₃N₄ catalysts under ambient conditions. Moreover, the formation energy (E_f) of Si@C₃N₄ was calculated as $E_f = \frac{1}{2}E_{N_2} + E_{Si@C_3N_4} - \mu_{Si} - E_{g-C_3N_4} = -0.08$ eV, where E_{N_2}, $E_{Si@C_3N_4}$, and $E_{g-C_3N_4}$ represent the total electronic energies of the N₂ molecule, the Si@C₃N₄ catalyst, and the pristine g-C₃N₄ nanosheet, respectively. μ_{Si} refers to the chemical potential of Si, obtained from $1/n*E_{Si-cell}$, suggesting the easy in-laboratory synthesis. Also, the interstitial Si-doping configuration, as shown in Fig. S2 (ESI†), was considered. A comparison between the two formation energies indicated that Si@C₃N₄ is more energetically favorable. Therefore, the subsequent concept catalysts of Si–M dimers were built on two N_{v1} sites, named SiM@C₃N₄.

Then, we examined the adsorption of N₂ on Si@C₃N₄. Fig. 1b exhibits two adsorption configurations of N₂, *i.e.*, end-on and side-on modes, and their corresponding N₂-induced charge density difference (CDD). The CDD shows that there exists noticeable electron transfer, *i.e.*, electron acceptance–backdonation, between the Si site and N₂, and the Hirshfeld charge analysis shows that N₂ obtains more electrons from the catalyst
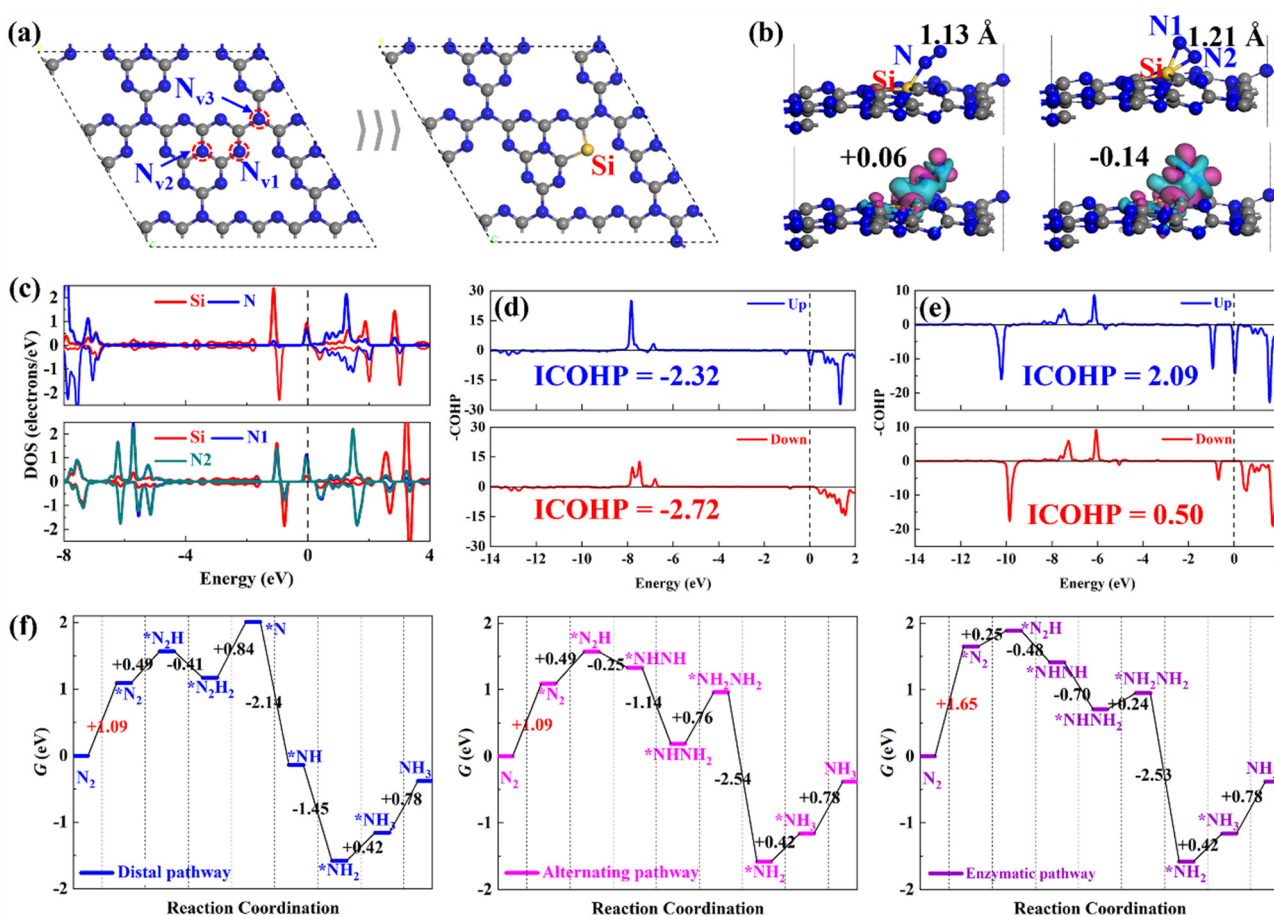

Fig. 1 Single Si dopped in g-C₃N₄ and the corresponding electronic structure and energy analyses: (a) schematic diagram of Si@C₃N₄ formation through N_{v1}; (b) two adsorption configurations and their corresponding charge density difference induced by N₂ adsorption with the red and cyan color representing the electron accumulation and loss, respectively (isosurface = 0.01 a.u.). Black values show the Hirshfeld charges of adsorbed N₂; (c) the Si–N electron interaction by DOS analysis; the −COHP and integrated −COHP analyses of the N–N bond from the end-on (d) and (e) side-on N₂ adsorption configurations; and (f) free energy evolutions through different reaction pathways. Color scheme: Si (yellow), N (blue), and C (grey).

13128 | *Phys. Chem. Chem. Phys.*, 2023, **25**, 13126–13135

This journal is © the Owner Societies 2023

in the side-on mode. The DOS results, shown in Fig. 1c, explain the electron interaction between Si and N: (1) N_2 is polarized after adsorption and (2) the electron interaction is stronger in the side-on mode. To obtain an intuitive comparison on the degree of activation of N≡N, the –COHP calculations were conducted for the end-on and side-on models, as shown in Fig. 1d and 1e. The –COHP analysis shows that there are more electrons occupied in the $1\pi^{\star}$ anti-bonding orbitals below the Fermi level in the side-on configuration, leading to the activation of N_2. The analysis of the N–N bond length, as displayed in Fig. 1b, describes the N≡N triple bond elongation to 1.13 and 1.21 Å, also in agreement with the –COHP results. However, the polarized $^{\star}N_2$ with more electrons occupying the $1\pi^{\star}$ orbital will increase the electronic energy. Fig. 1f shows the free energy evolutions of the ENRR starting from free N_2 to the NH_3 product (reaction mechanisms[53,54] refer to Fig. S1, ESI†), from which we can see that the adsorption of N_2 presents a significant barrier to the reaction, with relatively large free energy changes of +1.09 and +1.65 eV. Such significant free energy changes are difficult to overcome under ambient conditions, indicating that the ENRR will not occur on $Si@C_3N_4$. Enhancing the N_2 adsorption will boost the ENRR performance.

3.2 N_2 adsorption on $SiM@C_3N_4$

Here, asymmetric dimer electrocatalysts ($SiM@C_3N_4$) were designed to address the low affinity of N_2 on active sites. We chose some high-performance ENRR transition metals (TMs) to cooperate with Si to capture N_2, and the metal elements selected are shown in Fig. 2a. Fig. 2b displays the design scheme of concept-$SiM@C_3N_4$ which involves using two N_{V1} vacancies on g-C_3N_4. The optimized $SiM@C_3N_4$ catalysts are shown in Fig. S3 (ESI†). According to E_b and $(E_{co.Si} + E_{co.M.})$ analyses of dimers (see Table S1, ESI†), it is anticipated that these $SiM@C_3N_4$ concept models all exhibit strong stability under ambient conditions.

Then N_2 adsorption on $SiM@C_3N_4$ was examined. Fig. 2c and 2d display two dimer models, i.e., $SiMo@C_3N_4$ and
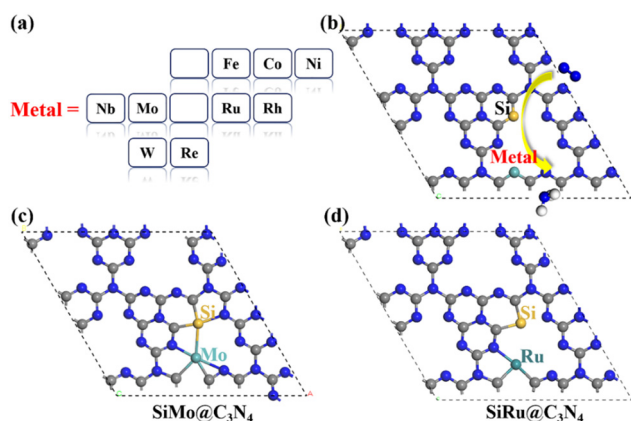

Fig. 2 (a) Chosen metal elements for the concept models of $SiM@C_3N_4$; (b) the design strategy of $SiM@C_3N_4$ for ENRR; (c and d) potential high-performance catalysts: $SiMo@C_3N_4$ and $SiRu@C_3N_4$. Color scheme: Si (yellow), H (white), N (blue), and C (grey).
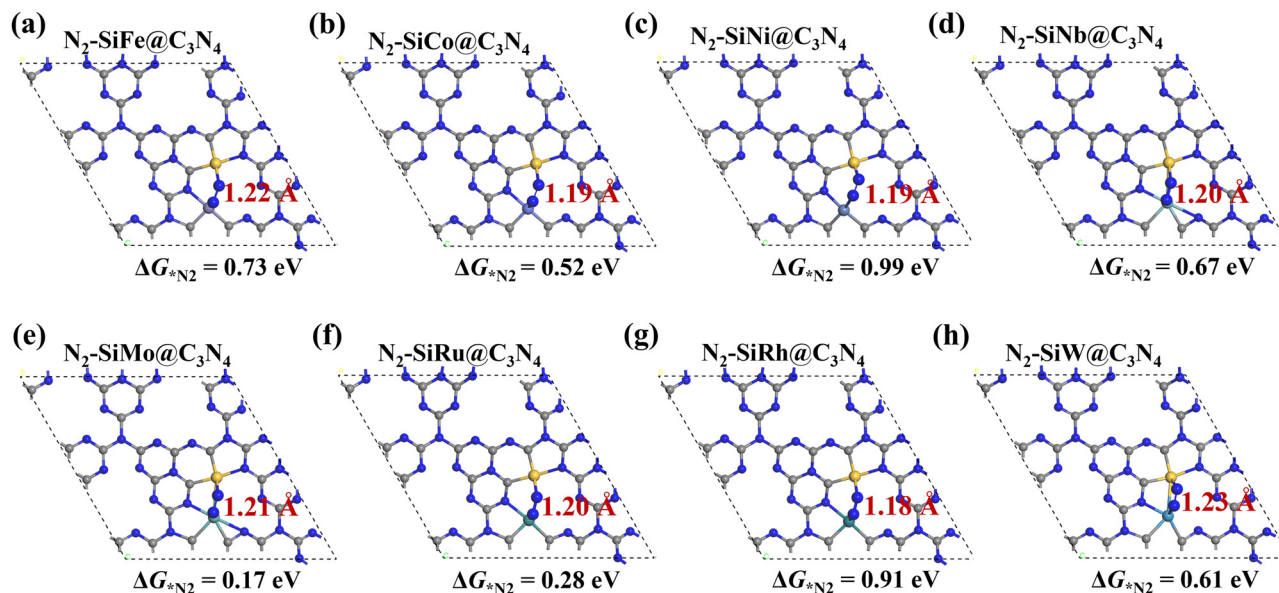
$SiRu@C_3N_4$. They all have strong N_2 adsorption ability with the adsorption free energy ($\Delta G_{\star N_2}$) less than 0.50 eV (see Fig. 3), indicating the occurrence possibility of N_2 adsorption under ambient conditions.[55,56] Fig. 3 displays the side-on adsorption configurations of N_2 on $SiM@C_3N_4$ except for $SiRe@C_3N_4$, because N_2 can only be captured in the end-on model at the Re site after geometry optimization as shown in Fig. S4 (ESI†). Among nine dimer concept-electrocatalysts, based on E_{ads} and adsorption-free energies ($\Delta G_{\star N_2}$), only two dimer catalysts were shown to have good N_2 adsorption ability, i.e., $SiMo@C_3N_4$ and $SiRu@C_3N_4$, with $\Delta G_{\star N_2}$ of 0.17 and 0.28 eV, respectively. Moreover, the side-on adsorption modes on $SiMo@C_3N_4$ and $SiRu@C_3N_4$ well-activated the adsorbed $^{\star}N_2$ with the extended N≡N lengths of 1.21 and 1.20 Å, respectively. However, other dimers showed $\Delta G_{\star N_2} > 0.50$ eV, indicating that N_2 adsorption under ambient conditions is challenging to overcome, although they all exhibited the activated characteristics due to the elongated N–N bond. To further analyze the adsorption process of N_2 on $SiM@C_3N_4$, the kinetic barriers were analyzed as shown in Fig. S5 (ESI†), from which it was noticed that N_2 adsorption barriers were all less than 0.50 eV except for $SiNi@C_3N_4$. $SiMo@C_3N_4$ and $SiRu@C_3N_4$ with the most energetically favorable $^{\star}N_2$ configurations demonstrated quite small reaction barriers of 0.23 and 0.24 eV, respectively. Therefore, from the perspective of adsorption thermodynamics and kinetics, N_2 can be readily activated on $SiMo@C_3N_4$ and $SiRu@C_3N_4$ under ambient conditions.

3.3 ENRR on $SiMo@C_3N_4$ and $SiRu@C_3N_4$

Following the discussion on N_2 adsorption above, we examined the ENRR performance on $SiMo@C_3N_4$ and $SiRu@C_3N_4$. According to relevant reports,[57,58] when N_2 is captured on dimer catalysts in a side-on mode, the ENRR generally can occur through two mechanisms, i.e., enzymatic and consecutive ones, which is schematically depicted in Fig. S6 (ESI†). Therefore, the ENRR on $SiMo@C_3N_4$ and $SiRu@C_3N_4$ was investigated according to the proposed mechanisms computationally.

Fig. 4 and Fig. S7 (ESI†) show the enzymatic and consecutive pathways on $SiMo@C_3N_4$ and $SiRu@C_3N_4$, respectively. For the first hydrogenation reduction step of $^{\star}N_2 + H^+ + e^- \rightarrow {}^{\star}N_2H$, there are two possible hydrogenation ways through the attack of the H^+/e^- pair (shown in Fig. S8, ESI†): one is to attack the N adatom bonded to Si and another is to attack the N adatom connected to the metal site. Based on free-energy analyses, the H^+/e^- pair energetically first tends to attack the N adatom bonded to the metal site. Likewise, on $SiMo@C_3N_4$, $^{\star}NH_3$ species also tend to form on the metal site; however, for $SiRu@C_3N_4$, $^{\star}NH_2$ and $^{\star}NH_3$ species can only form on the Si site. Fig. 5 demonstrates their corresponding free energy evolutions along enzymatic and consecutive pathways, from which we can notice that the PDS is the first hydrogenation step. Due to the well-activated N–N bond of $^{\star}N_2$, free-energy changes during the first hydrogenation steps on these two asymmetrical dimer centers, i.e., $SiMo@C_3N_4$ and $SiRu@C_3N_4$, are pretty low. The limiting potentials (U_L) on $SiMo@C_3N_4$ and $SiRu@C_3N_4$ are merely −0.20 and −0.39 V, respectively, for the ENRR, with the

This journal is © the Owner Societies 2023

Phys. Chem. Chem. Phys., 2023, **25**, 13126–13135 | **13129**

Fig. 3 (a–h) Side-on adsorption configurations of *N_2 on SiM@C_3N_4 with adsorption-free energies (ΔG_{*N_2}) and N–N bond lengths. N_2 adsorption configuration on SiRe@C_3N_4 is shown in Fig. S4 (ESI†).
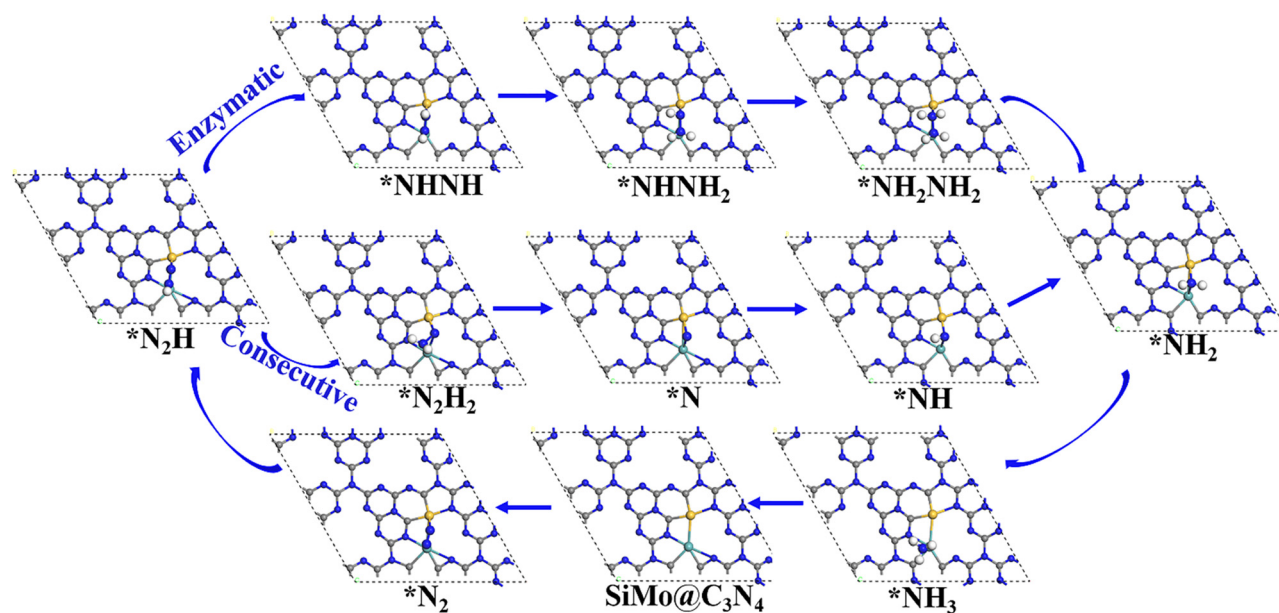

Fig. 4 The enzymatic and consecutive pathways of the ENRR on SiMo@C_3N_4, and the ENRR on SiRu@C_3N_4 is shown in Fig. S7 (ESI†).

responding overpotentials (η) of 0.04 and 0.23 V, respectively. Such low overpotentials indicate that the ENRR can be boosted under an ultra-low external potential. Moreover, these two dimers show comparable and even better performance than the reported metal-based electrocatalysts (FeV@C_2N:[59] U_L = −0.17 V; NbB:[60] U_L = −0.40 V; MnB:[60] U_L = −0.33 V; Mo and W-doped Au-based single-atom alloyes:[61] U_L = −0.30 V; Mo@BM-β_{12}:[62] U_L = −0.26 V; and Mn@BM-β_{12}:[62] U_L = −0.32 V;), even outperform some 2D Mxenes[63] (Mo$_2$C(OH)$_2$: U_L = −0.62 V; V$_2$C(OH)$_2$: U_L = −0.71 V; and Cr$_2$C(OH)$_2$: U_L = −0.78 V) and TM

single-atom catalysts[45,64] (Mo$_1$/pyrrolic-N$_3$-G: U_L = −0.49 V, Re$_1$/pyrrolic-N$_3$-G: U_L = −0.51 V; and Nb@P$_3$-Ars: U_L = −0.52 V), exhibiting a great promising prospect towards electrocatalytic nitrogen fixation.

ENRR on Mo@C_3N_4 and Ru@C_3N_4

Single-atom catalysts (SACs) have been the front line for upgrading ENRR electrocatalysts due to their peculiar properties, such as high-atom utilization, low-coordination sites, and tunable electronic properties. However, sometimes SACs suffer
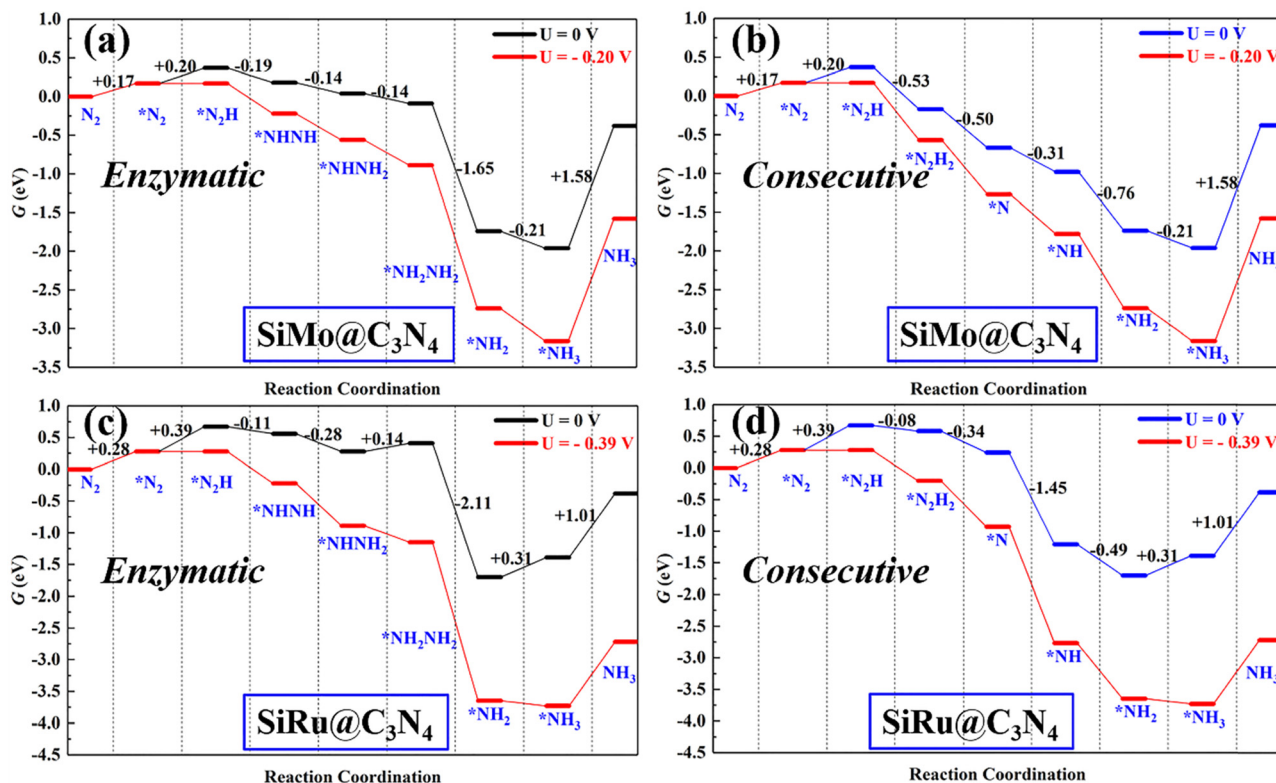
Fig. 5 The free energy evolutions of enzymatic and consecutive pathways on (a and b) SiMo@C_3N_4 and (c and d) SiRu@C_3N_4 with and without the applied potential (U_L).

from the limitation of scaling relationship during the ENRR, *i.e.*, less flexibility to meet all energetic requirements of multiple proton-coupled electron-transfer steps by tuning the electronic structures. Therefore, dual active sites may provide a solution to this issue.

For comparison with dimer catalysts, here ENRR performance on TM single-atom Mo@C_3N_4 and Ru@C_3N_4 (see Fig. S9–S11, ESI†) catalysts was also investigated. First, N_2 adsorption on Mo@C_3N_4 and Ru@C_3N_4 was also studied and is shown in Fig. S10 (ESI†). One can find that, on Mo@C_3N_4, the end-on adsorption configuration with $\Delta G_{*N_2} = -0.20$ eV is more favorable energetically than the side-on mode with $\Delta G_{*N_2} = 0.56$ eV, while as for Ru@C_3N_4, N_2 can be chemically adsorbed on the Ru site only in the end-on mode with $\Delta G_{*N_2} = 0.33$ eV. Therefore, tasking the N_2 end-on adsorption modes on both SACs as starting points, the ENRR along the distal and alternating pathway was investigated as shown in Fig. S11 (ESI†). Their corresponding free-energy evolutions are presented in Fig. 6, from which again we noticed that the first hydrogenation step (*N_2 + H^+ + e^- → *N_2H) is the PDS, with ΔG of 0.78 and 0.89 eV, for Mo@C_3N_4 and Ru@C_3N_4, respectively. As a result, the limiting potentials on Mo@C_3N_4 and Ru@C_3N_4 are -0.78 and -0.89 V, respectively, which are distinctly greater than those on SiMo@C_3N_4 and SiRu@C_3N_4 dimer catalysts. Generally, the first hydrogenation step is determined from the activation degree of *N_2 on electrocatalysts. This suggests that dimer catalysts possess a superb activity in the ENRR than

SACs, demonstrating the synergistic advantage of the combination of Si and metal sites (Mo/Ru) in N_2 adsorption and activation.

3.5 Origin of high-performance dimers

For studying the high-performance origin of SiMo@C_3N_4 and SiRu@C_3N_4, we investigated their electronic structures, as shown in Fig. 7. First, the calculated charge density difference (Fig. 7a) suggests that N_2 has a stronger electron exchange on SiM@C_3N_4 than on M@C_3N_4, and the Hirshfeld charge analysis (Table S2, ESI†) proved it quantitatively. The DOS data demonstrate the electron interaction around the Fermi level, and the strong electron exchange between N_2 and SiM@C_3N_4 resulted in splitting of the 1π molecular-orbital (MO). As for the N_2 adsorption on Mo@C_3N_4 and Ru@C_3N_4, the DOS overlap between the metal site and N_2 below the Fermi level was very small, suggesting a weaker electron interaction. This is also in accordance with the N–N bond length and electron density analyses (Fig. 7a). The COHP, offering an atom pair's chemical bonding and anti-bonding information, is a visual bonding indicator. Thus, the COHP analysis was performed for *N_2, as shown in Fig. 7c. Indeed, a larger electron occupation in the $1\pi^*$ orbital for side-on adsorption configurations on SiM@C_3N_4 was observed, and ICOHP results are on the order of -11.72 (*N_2 on SiRu@C_3N_4) < -10.32 (*N_2 on SiMo@C_3N_4), -4.37 (*N_2 on Ru@C_3N_4) < -4.08 (*N_2 on Mo@C_3N_4), quantitatively explaining the activation degree. The larger activation degree of N_2 is

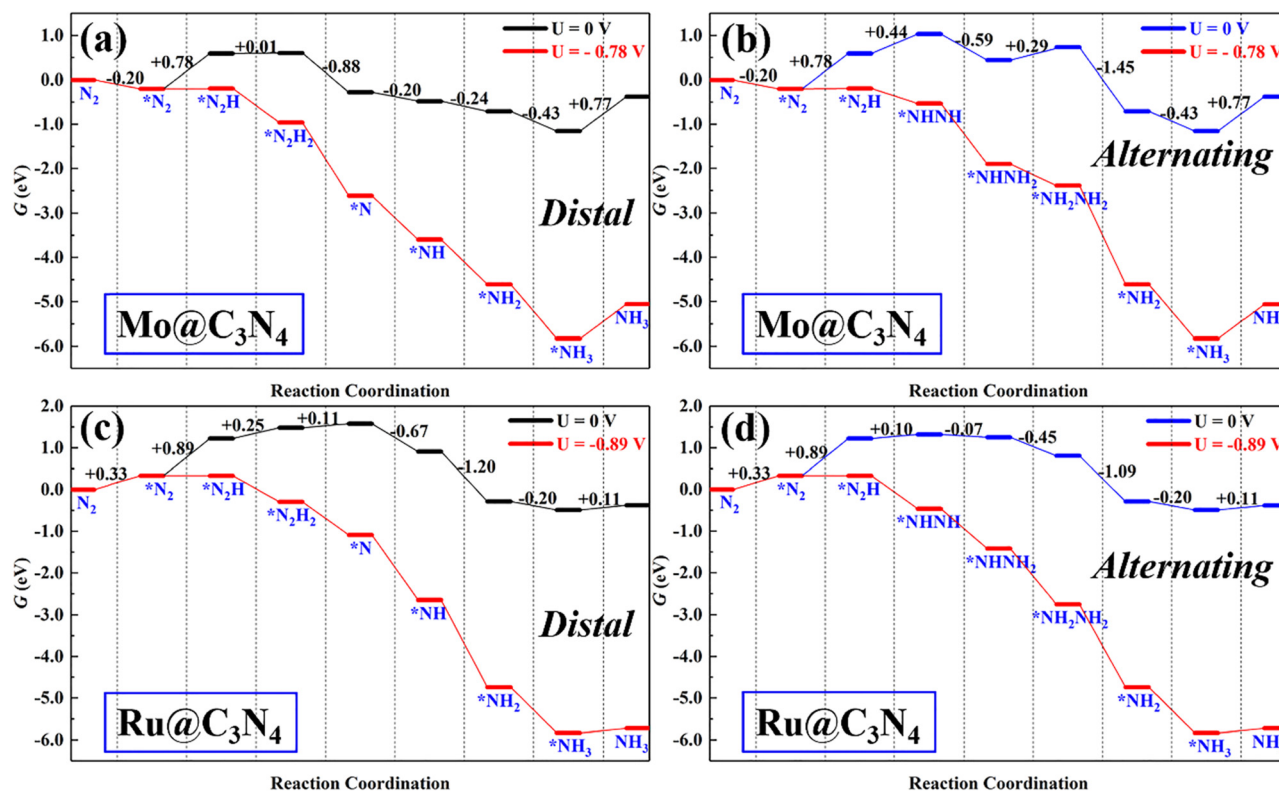This journal is © the Owner Societies 2023

Phys. Chem. Chem. Phys., 2023, **25**, 13126–13135 | **13131**

Fig. 6 The free energy evolution of the ENRR on (a and b) Mo@C$_3$N$_4$ and (c and d) Ru@C$_3$N$_4$.
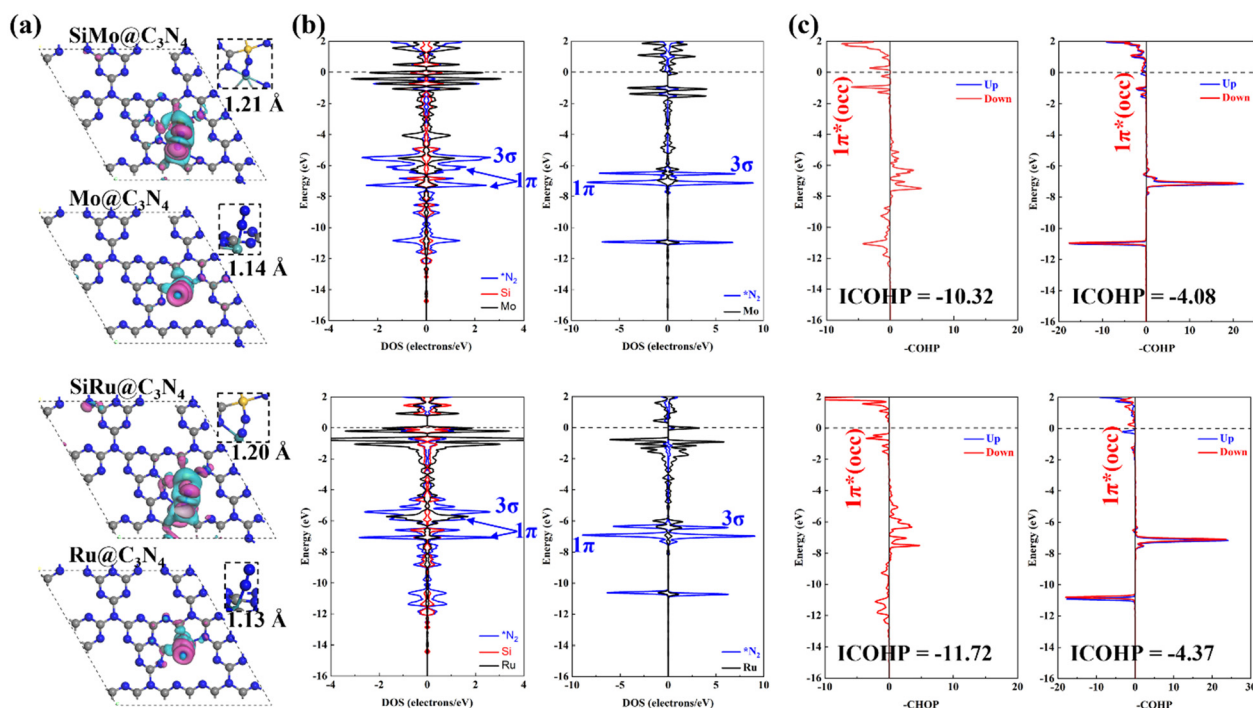

Fig. 7 Analyses of the electronic structure: (a) the DFT-calculated charge density difference induced by N$_2$ adsorption with the N−N bond length, and the red and cyan represent the electron accumulation and loss, respectively (isosurface = 0.01 a.u.); (b) DOS analyses for *N$_2$, Si, Mo, and Ru of four concept-models; and (c) the −COHP analyses for *N$_2$, where ''1π* (occ)'' refers to the occupation of 1π* anti-bonding orbitals.

conducive to decreasing the free energy of the first hydrogenation step.

Besides, the electron transfer between reaction intermediates and active sites also plays a crucial role during the hydrogenation process. Thus, we analyzed the Hirshfeld charge evolution of the ENRR on SiM@C_3N_4 and M@C_3N_4 (M = Mo and Ru) as shown in Fig. S13 (ESI†). Here, we analyzed Hirshfeld charges of four moieties on SiM@C_3N_4 (M = Mo and Ru) and three moieties on M@C_3N_4 (M = Mo and Ru): N_xH_y, (the reaction intermediates), Si (the non-metal site), Mo/Ru (the metal site) and defective g-C_3N_4 (the supporter structure). First, on SiMo@C_3N_4 (see Fig. S13a, ESI†), the charge evolution of N_xH_y was different from that of g-C_3N_4, and obvious charge oscillation for both N_xH_y and g-C_3N_4 could be observed. However, the charges on active sites (Si and Mo) oscillate slightly, and even the charge on Mo remains almost unchanged along the reaction coordinate. These findings suggest that g-C_3N_4 serves as the electron reservoir, and the active sites (Si and Mo) act as the electron adaptors. Similar results can also be obtained on SiRu@C_3N_4 (see Fig. S13c, ESI†). Additionally, these two active sites of SiM@C_3N_4 (M = Mo and Ru) could slightly regulate the charges on N_xH_y as a mediator during the synthesis of second ammonia. But, as for single-atom Mo@C_3N_4 and Ru@C_3N_4 (see Fig. S13b and d, ESI†), only the metal site can transfer electrons back and forth between g-C_3N_4 and N_xH_y intermediates. And the active site (Mo/Ru) mainly acts as an electron adaptor during the ENRR process because of almost unchanged Hirshfeld charges on them.

3.6 Hydrogen evolution reaction

The HER is parasitic in electrocatalysis, which can primarily consume electrons and reduce the selectivity of ammonia during the ENRR. The HER is a common issue in electrocatalysis, and many electro-chemical reduction reactions, including but not limited to carbon dioxide reduction,[65,66] nitrate reduction,[67] and nitrogen reduction. A suitable catalyst should not only have high activity but also possess decent selectivity. Here, adsorption of *H on two potential active sites of dimer catalysts, *i.e.*, Si and M (M = Mo/Ru), was examined as shown in Fig. 8a and 8b. We can find that ΔG_{max}^{HER} on SiMo@C_3N_4 is larger than ΔG_{max}^{NRR} (0.20 eV), and ΔG_{max}^{HER} on SiRu@C_3N_4 is also larger than ΔG_{max}^{NRR} (0.39 eV), which suggests that the HER will be suppressed due to the hindered Heyrovskey step (*H + H$^+$ + e^- → H_2). Therefore, the ENRR is energetically more favorable compared to the HER. Therefore, SiMo@C_3N_4 and SiRu@C_3N_4 would have high ammonia selectivity.

In addition, the water molecules in electrolytes may affect the N_2 adsorption. Therefore, water adsorption was also studied, as shown in Fig. 8c and d. In comparison with the N_2 adsorption, we can notice that the Mo site on SiMo@C_3N_4 will be occupied by H_2O due to a lower adsorption free-energy of −0.45 eV, which will adversely influence the nitrogen activation and reduction; while SiRu@C_3N_4 tends to adsorb N_2 rather than H_2O due to the lower adsorption free energy (0.33 eV) than that (0.35 and 0.72 eV) of H_2O. This indicates that SiRu@C_3N_4 will exhibit high activity and selectivity towards the ENRR, while SiMo@C_3N_4 will favor the ENRR in electrolytes
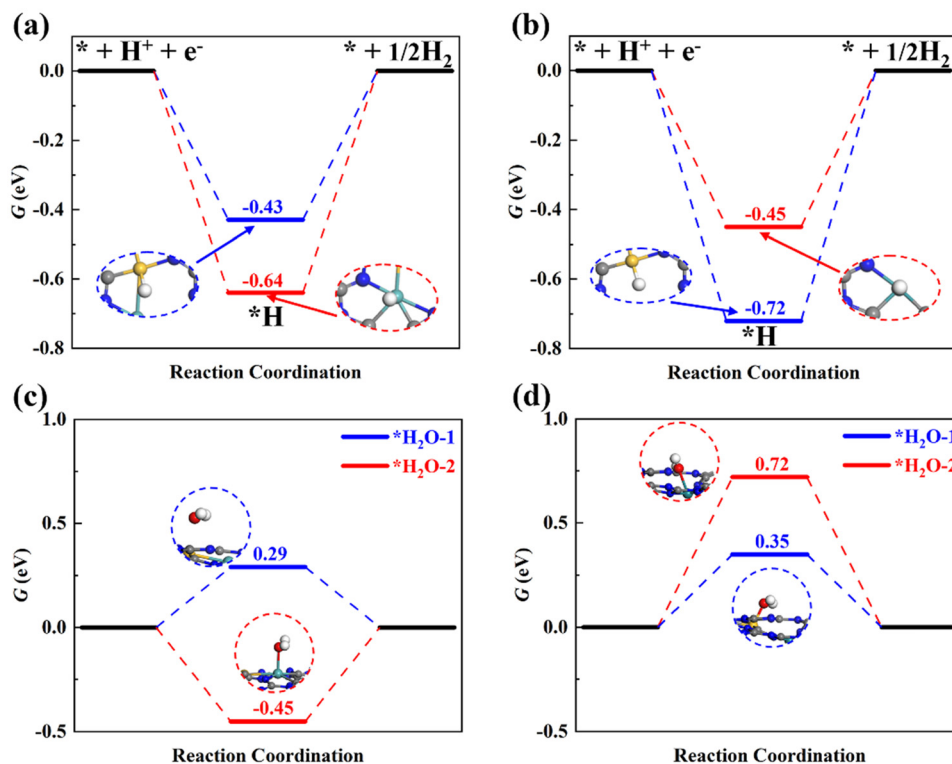

Fig. 8 Hydrogen evolution reaction on (a) SiMo@C_3N_4 and (b) SiRu@C_3N_4; the adsorption free energies of H_2O on (c) SiMo@C_3N_4 and (d) SiRu@C_3N_4. Note that there are two potential active sites on dimer catalysts for hydrogen and water adsorption.

This journal is © the Owner Societies 2023

Phys. Chem. Chem. Phys., 2023, **25**, 13126–13135 | **13133**

with a low concentration of H_2O, for example, ionic liquids.[68] To evaluate the synthetic availability of SiMo@C_3N_4 and SiRu@C_3N_4 with high activity in the laboratory, their formation energy was analyzed, which was found to be 2.19 and 1.36 eV, respectively, which means that both of them can be synthesized using some precursors and SiRu@C_3N_4 is easier to synthesize. Meanwhile, we designed another two models, SiMo-C_3N_4 and SiRu-C_3N_4 (see Fig. S14, ESI†), which are derived by directly doping two atoms into the holes of g-C_3N_4 nanosheets. By comparing their formation energies (Table S3, ESI†), we can see that the concept models of SiMo@C_3N_4 and SiRu@C_3N_4 are easier to synthesize. Therefore, again it is shown that the N_v site is a perfect anchoring site for atomic catalysts.

Conclusion

To sum up, asymmetrical dimer electrocatalysts were designed to realize the ENRR efficiently. Among the investigated SiM@C_3N_4 catalyst models, SiMo@C_3N_4 and SiRu@C_3N_4 exhibited the highest activity towards the ENRR with strong N_2 adsorption abilities and ultra-low onset potentials of −0.20 and −0.39 V, respectively. Moreover, these catalysts are capable of suppressing the competitive HER. Especially, SiRu@C_3N_4 exhibiting strong hydrophobicity possesses high NH_3 selectivity. This design strategy not only addresses the issue of low adsorption and activation ability towards N_2 on Si but also opens up a new avenue for designing asymmetrical dimer electrocatalysts for the ENRR, with the advantage of metal-based and non-metal-based catalysts.

Conflicts of interest

The authors declare that they have no known competing financial interests or personal relationships that could have appeared to influence the work reported in this paper.

Acknowledgements

References

1 X. Zhu, S. Mou, Q. Peng, Q. Liu, Y. Luo, G. Chen, S. Gao and X. Sun, *J. Mater. Chem. A*, 2020, **8**, 1545–1556.

2 D. Hao, Y. Liu, S. Gao, H. Arandiyan, X. Bai, Q. Kong, W. Wei, P. K. Shen and B.-J. Ni, *Mater. Today*, 2021, **46**, 212–233.

3 Y. Wen, H. Zhu, J. Hao, S. Lu, W. Zong, F. Lai, P. Ma, W. Dong, T. Liu and M. Du, *Appl. Catal., B*, 2021, **292**, 120144.

4 W. Liao, L. Qi, Y. Wang, J. Qin, G. Liu, S. Liang, H. He and L. Jiang, *Adv. Funct. Mater.*, 2021, 2009151.

5 W. Zhang, J. Low, R. Long and Y. Xiong, *Energy Chem.*, 2020, **2**, 100040.

6 L. Niu, L. An, X. Wang and Z. Sun, *J. Energy Chem.*, 2021, **61**, 304–318.

7 H. Liu, *Chin. J. Catal.*, 2014, **35**, 1619–1640.

8 L. Shi, Q. Li, C. Ling, Y. Zhang, Y. Ouyang, X. Bai and J. Wang, *J. Mater. Chem. A*, 2019, **7**, 4865–4871.

9 J. Zhao, X. Ren, X. Li, D. Fan, X. Sun, H. Ma, Q. Wei and D. Wu, *Nanoscale*, 2019, **11**, 4231–4235.

10 P. Song, L. Kang, H. Wang, R. Guo and R. Wang, *ACS Appl. Mater. Interfaces*, 2019, **11**, 12408–12414.

11 Y. Li, D. Gao, S. Zhao, Y. Xiao, Z. Guo, Y. Fang, J. Lin, Z. Liu, Y. Huang, K. Guo and C. Tang, *Chem. Eng. J.*, 2021, **410**, 128419.

12 Z. Guo, S. Qiu, H. Li, Y. Xu, S. J. Langford and C. Sun, *Diamond Relat. Mater.*, 2021, **111**, 108210.

13 Z. Guo, S. Qiu, H. Li, Y. Xu, S. J. Langford and C. Sun, *Phys. Chem. Chem. Phys.*, 2020, **22**, 21761–21767.

14 C. Liu, Q. Li, C. Wu, J. Zhang, Y. Jin, D. R. MacFarlane and C. Sun, *J. Am. Chem. Soc.*, 2019, **141**, 2884–2888.

15 J. Zhao, B. Wang, Q. Zhou, H. Wang, X. Li, H. Chen, Q. Wei, D. Wu, Y. Luo, J. You, F. Gong and X. Sun, *Chem. Commun.*, 2019, **55**, 4997–5000.

16 J. Zhao, J. Yang, L. Ji, H. Wang, H. Chen, Z. Niu, Q. Liu, T. Li, G. Cui and X. Sun, *Chem. Commun.*, 2019, **55**, 4266–4269.

17 L. Xia, X. Wu, Y. Wang, Z. Niu, Q. Liu, T. Li, X. Shi, A. M. Asiri and X. Sun, *Small Methods*, 2018, **3**, 1800251.

18 L. Xia, J. Yang, H. Wang, R. Zhao, H. Chen, W. Fang, A. M. Asiri, F. Xie, G. Cui and X. Sun, *Chem. Commun.*, 2019, **55**, 3371–3374.

19 G.-Y. Zhai, D. Xu, S.-N. Zhang, Z.-H. Xue, H. Su, Q.-Y. Yu, H.-H. Wang, X. Lin, Y.-X. Lin, L.-H. Sun, X.-H. Li and J.-S. Chen, *Adv. Funct. Mater.*, 2020, **30**, 2005779.

20 Z. Guo, S. Qiu, H. Li, Y. Xu, S. J. Langford and C. Sun, *ChemCatChem*, 2021, **13**, 1239–1245.

21 Z. Guo, T. Wang, H. Liu, S. Qiu, X. Zhang, Y. Xu, S. J. Langford and C. Sun, *Nanoscale*, 2022, **14**, 5782–5793.

22 Y. Luo, M. Li, Y. Dai, X. Zhang, R. Zhao, F. Jiang, C. Ling and Y. Huang, *J. Mater. Chem. A*, 2021, **9**, 15217–15225.

23 T. He, A. R. P. Santiago, Y. Kong, M. A. Ahsan, R. Luque, A. Du and H. Pan, *Small*, 2022, **18**, 2106091.

24 X. Sun, Y. Qiu, B. Jiang, Z. Chen, C. Zhao, H. Zhou, L. Yang, L. Fan, Y. Zhang and N. Zhang, *Nat. Commun.*, 2023, **14**, 291.

25 D. Wu, B. He, Y. Wang, P. Lv, D. Ma and Y. Jia, *J. Phys. D: Appl. Phys.*, 2022, **55**, 203001.

26 Y. Ouyang, L. Shi, X. Bai, Q. Li and J. Wang, *Chem. Sci.*, 2020, **11**, 1807–1813.

27 T. He, K. Reuter and A. Du, *J. Mater. Chem. A*, 2020, **8**, 599–606.

13134 | *Phys. Chem. Chem. Phys.*, 2023, **25**, 13126–13135

This journal is © the Owner Societies 2023

28 M. Groenewolt and M. Antonietti, *Adv. Mater.*, 2005, **17**, 1789–1792.

29 W. Wang, H. Zhang, S. Zhang, Y. Liu, G. Wang, C. Sun and H. Zhao, *Angew. Chem., Int. Ed.*, 2019, **58**, 16644–16650.

30 H. Ma, Z. Shi, S. Li and N. Liu, *Appl. Surf. Sci.*, 2016, **379**, 309–315.

31 C. Ren, Y. Zhang, Y. Li, Y. Zhang, S. Huang, W. Lin and K. Ding, *J. Phys. Chem. C*, 2019, **123**, 17296–17305.

32 C. Lv, Y. Qian, C. Yan, Y. Ding, Y. Liu, G. Chen and G. Yu, *Angew. Chem., Int. Ed.*, 2018, **57**, 10246–10250.

33 Z. Chen, J. Zhao, C. R. Cabrera and Z. Chen, *Small Methods*, 2018, **3**, 1800368.

34 X. Li, X. Sun, L. Zhang, S. Sun and W. Wang, *J. Mater. Chem. A*, 2018, **6**, 3005–3011.

35 G. Dong, W. Ho and C. Wang, *J. Mater. Chem. A*, 2015, **3**, 23435–23441.

36 K. Chu, Q.-q Li, Y.-p Liu, J. Wang and Y.-h Cheng, *Appl. Catal., B*, 2020, **267**, 118693.

37 K. Wang, Q. Li, B. Liu, B. Cheng, W. Ho and J. Yu, *Appl. Catal., B*, 2015, **176–177**, 44–52.

38 H. Xie, Y. Zheng, X. Guo, Y. Liu, Z. Zhang, J. Zhao, W. Zhang, Y. Wang and Y. Huang, *ACS Sustainable Chem. Eng.*, 2021, **9**, 6788–6798.

39 D. Jiao, Y. Liu, Q. Cai and J. Zhao, *J. Mater. Chem. A*, 2021, **9**, 1240–1251.

40 J. Zhang, X. Tian, M. Liu, H. Guo, J. Zhou, Q. Fang, Z. Liu, Q. Wu and J. Lou, *J. Am. Chem. Soc.*, 2019, **141**, 19269–19275.

41 S. Mukherjee, X. Yang, W. Shan, W. Samarakoon, S. Karakalos, D. A. Cullen, K. More, M. Wang, Z. Feng, G. Wang and G. Wu, *Small Methods*, 2020, **4**, 1900821.

42 Z. Zhang and X. Xu, *ACS Appl. Mater. Interfaces*, 2020, **12**, 56987–56994.

43 Q. Li, L. He, C. Sun and X. Zhang, *J. Phys. Chem. C*, 2017, **121**, 27563–27568.

44 C. Liu, Q. Li, J. Zhang, Y. Jin, D. R. MacFarlane and C. Sun, *J. Mater. Chem. A*, 2019, **7**, 4771–4776.

45 W. Zhao, L. Chen, W. Zhang and J. Yang, *J. Mater. Chem. A*, 2021, **9**, 6547–6554.

46 D. Ma, Z. Zeng, L. Liu and Y. Jia, *J. Energy Chem.*, 2021, **54**, 501–509.

47 A. Tkatchenko and M. Scheffler, *Phys. Rev. Lett.*, 2009, **102**, 073005.

48 E. Skúlason, T. Bligaard, S. Gudmundsdóttir, F. Studt, J. Rossmeisl, F. Abild-Pedersen, T. Vegge, H. Jónsson and J. K. Nørskov, *Phys. Chem. Chem. Phys.*, 2012, **14**, 1235–1245.

49 J. K. Nørskov, J. Rossmeisl, A. Logadottir, L. Lindqvist, J. R. Kitchin, T. Bligaard and H. Jónsson, *J. Phys. Chem. B*, 2004, **108**, 17886–17892.

50 H.-J. Chun, V. Apaja, A. Clayborne, K. Honkala and J. Greeley, *ACS Catal.*, 2017, **7**, 3869–3882.

51 G. Henkelman and H. Jónsson, *J. Chem. Phys.*, 2000, **113**, 9978–9985.

52 Q. Tay, P. Kanhere, C. F. Ng, S. Chen, S. Chakraborty, A. C. H. Huan, T. C. Sum, R. Ahuja and Z. Chen, *Chem. Mater.*, 2015, **27**, 4930–4933.

53 X. Cui, C. Tang and Q. Zhang, *Adv. Energy Mater.*, 2018, **8**, 1800369.

54 S. L. Foster, S. I. P. Bakovic, R. D. Duda, S. Maheshwari, R. D. Milton, S. D. Minteer, M. J. Janik, J. N. Renner and L. F. Greenlee, *Nat. Catal.*, 2018, **1**, 490–500.

55 Q. Liu, S. Wang, G. Chen, Q. Liu and X. Kong, *Inorg. Chem.*, 2019, **58**, 11843–11849.

56 Y. Abghoui and E. Skúlason, *Catal. Today*, 2017, **286**, 69–77.

57 L. J. Arachchige, Y. Xu, Z. Dai, X. L. Zhang, F. Wang and C. Sun, *J. Mater. Sci. Technol.*, 2021, **77**, 244–251.

58 D. Ma, Z. Zeng, L. Liu, X. Huang and Y. Jia, *J. Phys. Chem. C*, 2019, **123**, 19066–19076.

59 W. Zhang and B.-W. Zhang, *Nano-Micro Lett.*, 2021, **13**, 106.

60 M. Zafari, A. S. Nissimagoudar, M. Umer, G. Lee and K. S. Kim, *J. Mater. Chem. A*, 2021, **9**, 9203–9213.

61 G. Zheng, Y. Li, X. Qian, G. Yao, Z. Tian, X. Zhang and L. Chen, *ACS Appl. Mater. Interfaces*, 2021, **13**, 16336–16344.

62 L. Xu, L.-M. Yang and E. Ganz, *ACS Appl. Mater. Interfaces*, 2021, **13**, 14091–14101.

63 X. Lv, L. Kou and T. Frauenheim, *ACS Appl. Mater. Interfaces*, 2021, **13**, 14283–14290.

64 R. Song, J. Yang, M. Wang, Z. Shi, X. Zhu, X. Zhang, M. He, G. Liu, G. Qiao and Z. Xu, *ACS Omega*, 2021, **6**, 8662–8671.

65 C. Liu, T. Wang, D. Hao, Q. Li, S. Li and C. Sun, *J. Mater. Sci. Technol.*, 2022, **110**, 96–102.

66 S. Jin, Z. Hao, K. Zhang, Z. Yan and J. Chen, *Angew. Chem., Int. Ed.*, 2021, **60**, 20627–20648.

67 Y. Wang, C. Wang, M. Li, Y. Yu and B. Zhang, *Chem. Soc. Rev.*, 2021, **50**, 6720–6733.

68 F. Zhou, L. M. Azofra, M. Ali, M. Kar, A. N. Simonov, C. McDonnell-Worth, C. Sun, X. Zhang and D. R. MacFarlane, *Energy Environ. Sci.*, 2017, **10**, 2516–2520.

This journal is © the Owner Societies 2023

Phys. Chem. Chem. Phys., 2023, **25**, 13126–13135 | **13135**